

Diffraction Magic Cube Network with Super-high Capacity Enabled by Mechanical Reconfiguration

Peijie Feng¹, Fubei Liu², Yuanfeng Liu², Mingzhe Chong¹, Zongkun Zhang¹, Qian Zhao³, Jingbo Sun², Ji Zhou², Yunhua Tan¹

¹School of Electronics, Peking University, Beijing, 100871, China

²State Key Laboratory of New Ceramics and Fine Processing, School of Materials Science and Engineering, Tsinghua University,

Beijing 100084, China

³State Key Laboratory of Tribology in Advanced Equipment, Department of Mechanical Engineering, Tsinghua University, Beijing,

China

These authors contribute equally: Peijie Feng & Fubei Liu

Correspondence: Yunhua Tan Email: tanggeric@pku.edu.cn & Ji Zhou Email: zhouji@tsinghua.edu.cn & Jingbo Sun Email:

jingbosun@mail.tsinghua.edu.cn

Peijie Feng Email: pjf@stu.pku.edu.cn

Fubei Liu Email: lfb23@mails.tsinghua.edu.cn

Yuanfeng Liu Email: lyf_student@126.com

Mingzhe Chong Email: cmz1999@stu.pku.edu.cn

Zongkun Zhang Email: zhangzongkun1998@163.com

Jingbo Sun Email: jingbosun@mail.tsinghua.edu.cn

Qian Zhao Email: zhaoqian@tsinghua.edu.cn

Abstract

Multiplexing and dynamic reconfigurable metasurfaces have been extensively studied to enhance optical system capacity in response to the challenges posed by the exponential growth of optical information. Among them, the mechanically reconfigurable strategy offers a cost-effective and low-complexity approach for capacity enhancement. However, the channel numbers achieved in current studies are insufficient for practical applications because of inadequate mechanical transformations and suboptimal optimization methods. In this article, a diffractive magic cube network (DMCN) is proposed to advance the multiplexing capacity of mechanically reconfigurable metasurfaces. We utilized the deep diffractive neural network (D²NN) model to jointly optimize the subset of channels generated by the combination of three mechanical operations, permutation, translation, and rotation. The 144-channel holograms, 108-channel single-focus/multi-focus, and 60-channel orbital angular momentum (OAM) beam/comb generation were numerically achieved and experimentally validated using a spatial light modulator (SLM) and a reflective mirror. Our strategy not only provides a novel paradigm to improve metasurface capacity to super-high level with low crosstalk, but also paves the way for new advancements in optical storage, computing, communication, and photolithography.

Introduction

Metasurfaces, ultrathin and efficient photonic devices enabling manipulation of light wavefronts at subwavelength scales, have provided powerful platforms for the development of novel optical information systems, including meta-holography^{1,2}, metalenses³, orbital angular momentum (OAM) beam generation⁴⁻⁶, optical computing⁷⁻⁹, optical storage¹⁰, etc. The information capacity of these systems needs to be continually enhanced to accommodate the ever-growing demands of massive information processing. In recent years, extensive studies on metasurface multiplexing strategies have been conducted to enhance system capacity. Early efforts successfully develop independent multiplexing channels leveraging wavelength^{2,11}, polarization¹²⁻¹⁴, OAM¹⁵, transmission direction¹⁶, and incident angle¹⁷ of light but these approaches provide limited channels (i.e., less than 4) due to the constraints on channel independence. Fortunately, Xiong et al. achieved 11 non-orthogonal polarization multiplexing channels by introducing correlated noise into the least squares algorithm²⁰. This breakthrough overcomes the design limitations of independent channels and demonstrates the possibility of multiplexing using correlated channels. Inspired by this work, an increasing number of studies have begun to explore the non-orthogonal polarization channels for multifunctional multiplexing¹⁸⁻²⁰. However, the correlation between multiple channels increases crosstalk, making the metasurface parameter design more challenging. D²NN, a data-driven deep learning optical network is frequently used in these researches to address the obstacle. The state-of-the-art work reported by Wang et al. utilized D²NN to jointly optimize 55 non-orthogonal polarization channels obtained by extending the dimension of the Jones matrix, achieving ultrahigh-capacity holography²¹.

Dynamic metasurfaces with reconfigurable or reprogrammable features are also widely adopted to enhance the system capacity. Common strategies for dynamically controlling the optical response of materials involve introducing the external stimuli, such as voltage^{22,23}, light²⁴, and temperature²⁵, through the design of active metasurfaces. These methods incorporate extra static bias components, including PIN diodes, photodiodes, and VO₂, into the metaatom, thereby increasing complexity, volume, and energy consumption of the metasurfaces. Mechanical reconfigurable metasurfaces, which alter the material structure through mechanical operations, offer a cost-effective and low-complexity solution for dynamic manipulation of light. Inspired by origami/kirigami arts, researchers alter the geometry of metaatom through folding or stretching to achieve reconfigurable chirality^{26,27}, tunable focusing^{28,29}, dynamic holographic³⁰. Since the shape of each metaatom undergoes restricted changes simultaneously through a single mechanical operation, these designs face challenges in further enhancing the number of channels. Instead, reconfiguring a layer within cascaded metasurfaces on a large scale via rotation or insertion provides a more flexible approach^{19,20,31-34}, with significant potential to enhance system capacity. However, the experimentally achieved channel numbers in current studies remain limited (i.e., fewer than 20) due to inadequate mechanical transformations and ineffective optimization models, which are far from meeting the demands of practical applications. The increased channel number also reduces the signal-to-noise ratio (SNR), and a trade-off between them has yet to be well established. Therefore, the ultimate limit for this type of coarse-grained reconfigurable mechanisms remains to be explored.

In this article, we introduce a diffractive magic cube network (DMCN) consisting of three cascaded layers, elevating the

multiplexing capacity of mechanically reconfigurable mechanisms to a super-high level. Our DMCN constructed thousands of non-independent potential channels through the combination of three coarse-grained mechanical operations: permutation, translation, and rotation. We carefully selected a subset of these channels and employed the D²NN model to optimize the transmission phases of the DMCN, achieving 144-channel holograms (PCC \sim 0.98), 108-channel single-focus/multi-focus (PCC \sim 0.89), and 60-channel OAM beam/comb generation (CC \sim 0.99). The interrelationships among the layer width, field of view (FOV) width, channel count and SNR were also analyzed in detail, revealing that an increased layer-to-FOV width ratio enhances channel capacity and SNR. The proof-of-concept validation was conducted using the combination of a spatial light modulator (SLM) and a reflective mirror to simulate mechanical operations, demonstrating good agreement between the experimental results and numerical simulations. Since the DMCN was implemented by the simplest isotropic phase-modulated cells, it can easily be integrated with techniques such as polarization multiplexing and wavelength multiplexing to further enhance channel count. Our strategy provides a novel paradigm for enhancing metasurface capacity, which involves constructing a large amount of non-independent channels across multiple dimensions and subsequently employing D²NN model for joint optimization. This work will provide new possibilities for the development of optical storage, display, encryption, photolithography³⁵ and optical communications^{36,37}.

Results

The super-high capacity and optimization of DMCN

The system schematic of our DMCN is shown in **Fig. 1**. We employed the forward propagation model of D²NN to describe the wave transfer procedure in the system. Specifically, the incident light is first modulated by the diffractive layer, and the resulting modulated wavefront then acts as a secondary wave source, radiating subwaves to the adjacent layer. This process is repeated three times, ultimately forming the target wavefield at the output FOV. A corresponding system transfer matrix \mathbf{A}_c (See **Methods** for details) was also derived to help demonstrate the reconfigurable mechanism of DMCN. Its parameters can be altered by three types of coarse-grained mechanical operations, enabling the generation of potential channels. Permutation operations change the order of the layers (e.g., ABC \rightarrow BAC), thereby altering the positions of the modulation coefficient matrices $\mathbf{T}_A, \mathbf{T}_B, \mathbf{T}_C$ in equation (e.g., $\mathbf{T}_1 = \mathbf{T}_A, \mathbf{T}_2 = \mathbf{T}_B, \mathbf{T}_3 = \mathbf{T}_C \rightarrow \mathbf{T}_1 = \mathbf{T}_B, \mathbf{T}_2 = \mathbf{T}_A, \mathbf{T}_3 = \mathbf{T}_C$). Rotation operations applied to the second and third layers modify the rotation angles of the matrices of \mathbf{T}_2 and \mathbf{T}_3 , denoted as Ω_1 and Ω_2 . Translation operations adjust the layer distances d_1, d_2, d_3 through shifting the second and third layers. Notably, the total longitudinal length, $d_1 + d_2 + d_3$, is designed as a const, allowing the optical information stored in the different mechanical states of the DMCN to be excited and directed to the fixed output FOV under the illumination of incident plane wave J .

Fig. 2 b illustrates the combination manners of aforementioned mechanical operations, which endows the DMCN with thousands of potential channels. The full permutations (i.e., $P_3^3 = 6$) and partial permutations (i.e., $P_3^2 + P_3^1 = 9$) of the three modulation layers generated 15 channels. The second and third layers of DMCN can be respectively rotated to four specific angles: $0^\circ, 90^\circ, 180^\circ$, and 270° , resulting in another 16 possible combinations. Lastly, the total longitudinal length of 30 cm was discretized into 60 intervals, each measuring 0.5 cm. The intervals allocated to d_1 and d_2 were equal to facilitate the experiment, which produced 29 possible configurations of interlayer distances for translation operations. These channels were combined to form a total of 4179 channels. It is noteworthy that these channels are not independent, as they share the trainable parameters $\mathbf{T}_A, \mathbf{T}_B, \mathbf{T}_C$. Any updates to these matrices simultaneously affect the transfer functions of all channels. To minimize crosstalk among these correlated channels as much as possible, we employed the backpropagation gradient descent algorithm of the D²NN model for joint optimization, as illustrated in **Fig. 2 a**. The transfer matrix of each channel, constructed by zero-initialized trainable coefficients, firstly transformed the input plane wave to output wavefield. Subsequently, the loss function of each channel computed the error between ground truth and field in output FOV. During each iteration (or epoch), losses of all channels to be optimized were summed for parameter updates through gradient descent. Utilizing minimum square error (MSE) or negative correlation (NC) loss function (see **Methods** for details), the carefully selected channels were optimized to achieve 144-channel holograms, 108-channel single-focus/multi-focus, 60-channel OAM beam/comb, respectively.

Numerical simulation results of reconfigurable holography

Multi-channel holography was initially taken as an example to demonstrate the effectiveness of the proposed mechanically reconfigurable strategy. By leveraging the single type of mechanical transformation, the pairwise combinations of transformations, and the integration of three transformations, the channel capacity of DMCN holography was progressively enhanced from 15 to 144. An MSE loss function with an efficiency regularization term was employed during DMCN training to optimize the image quality while controlling system efficiency. The ground truth of the quick draw, expression, and letter images used for training is presented in the **Supplementary Figs. 19-21**. To assess the hologram quality, the Pearson correlation coefficient (PCC) was used to evaluate the similarity between the output holograms and ground truth images, while the peak signal-to-noise ratio (PSNR) was used to analyze the noise intensity in the holograms. Detailed definitions of these metrics are provided in the **Methods** part. **Supplementary Figs. 1-3** present simulation results of multi-channel quick draw holograms respectively achieved by translation (16 channels), permutation (15 channels), and rotation (16 channels). The PCC values of these holograms are 1, indicating negligible differences from the target images.

Supplementary Figs. 4 a-c show the simulation results of multi-channel expression holography obtained from pairwise combinations of the three mechanical operations selected in **Fig. 2 b**. Specifically, the 18-channel holography was achieved by combining translation with permutation, the 24-channel holography by combining translation with rotation, and the 48-channel holography by combining rotation with permutation. The layer width and output FOV width of these DMCNs were respectively configured as 300 and 120. To balance the trade-off between image quality and system efficiency caused by the iterative spatial filtering process in the DMCN model, we adopted a strategy of reducing imaging efficiency to maintain high image clarity as the channel count increases. Therefore, the target optimization efficiency η_{Th} was respectively set to 18%, 16%, and 12% when training these models. Both the holographic images and evaluation metrics indicate that the image quality remains high despite the increased channel count. The PCCs maintain around 0.99, and the PSNRs stay near 19.9 dB. The high-fidelity results of the 48-channel holography demonstrate that the multiplexed channels enabled by combining two mechanical operations can be fully optimized, indicating significant potential for further system capacity enhancement.

Fig. 2 c-e present the simulation results of 144-channel letter holography achieved through a complete integration of the three types of mechanical operations. To keep high image quality, the value of η_{Th} was further reduced to 4.5%, and the output FOV width was reduced to 85. The detailed relationships among image PSNR, channel number, layer width and FOV width ratio are analyzed in the “**The model scalability of DMCN**” part. The holographic images demonstrate consistent image fidelity across all channels, with minimal variation. Their PCCs show a mean of 0.98, ranging from 0.972 to 0.986, and their PSNRs have a mean of 22.8 dB, spanning from 20.2 dB to 26.4 dB, reflecting the high imaging quality of system. These results from reconfigurable holography conclusively underscore the super-high information capacity of our DMCN.

Numerical simulation results of reconfigurable single-focus/multi-focus

To further explore the application potential of our DMCN model, we also optimized it to achieve multi-channel single-focus/multi-focus. The model layer width and output FOV width were both set to 300 for this scenario. During model training, the same loss function used in DMCN holography was utilized and η_{Th} was set to 4%. The optimization target was set as focused patterns consisting of small squares centered around the target focal points. The side length of these squares could determine the full width at half maximum (FWHM) of the output Airy disks. On one hand, an excessively large side length will cause the output wavefield of the DMCN to fail in properly focusing on the target region, leading to energy dispersion. On the other hand, a too small side length will result in focal points with overly narrow FWHMs, thereby reducing focusing efficiency. Therefore, a single-layer meta-lens was chosen as a benchmark to determine the optimal side length of the target squares. **Supplementary Fig. 5** shows the phase profile of a meta-lens with the same layer width and sampling interval as the DMCN. Its focal length matches the longitudinal length of the DMCN, with a numerical aperture of 0.0062. The FWHM of its focal point is 36.25 μm , approximately 3 sampling intervals. Thus, the side length of our focused squares was set to 3 pixels (37.5 μm). To avoid excessively low focusing efficiency, a total of 108 channels were selected for joint optimization. These channels are derived from the combination of the first six rotation channels and the other two types of channels shown in **Fig. 2**

b. Among them, 64 channels were allocated for single-focus, 20 for dual-focus, 16 for triple-focus, and 8 for quad-focus. The target focusing patterns for these configurations are presented in **Supplementary Fig. 22**.

Fig. 3 a illustrates the 108-channel output focusing wavefields of the well-trained DMCN. The output field of each channel is effectively concentrated in its target focal region, with high channel isolation and no crosstalk occurring. **Fig. 3 b** presents the histograms of evaluation metrics for multi-channel DMCN focusing. The mean PCC is 0.89, which is lower than the average value observed in multi-channel holography. The PCCs are reduced due to the fact that the output focal points are Airy disks, while the evaluation targets are squares. The FWHMs of most focal points are around 33.5 μm , slightly smaller than the predesigned side length of the square patterns. For focusing efficiency, we defined the focusing energy as the total energy within three times the FWHM of the focal point and calculated an average efficiency of 2.9% across 108 channels.

Seven example channels were additionally selected to provide a more detailed illustration of the focusing results. The output fields of these channels are represented by their one-dimensional horizontal profiles and two-dimensional cross-sections at the focal height, as shown in **Fig. 3 c** and **Fig. 3 d**. These channels involve single-focus channels 1 and 29, dual-focus channels 75 and 83, triple-focus channels 93 and 97, and quad-focus channel 107. The one-dimensional curves of all channels exhibit a maximum at the target focal point, and the relative field intensity rapidly diminishes to near zero as the distance from the maximum increases. When the number of focal points increases to 3 or 4, relative intensity at each focal point exhibits slight differences, with a variation of approximately 0.1. The two-dimensional field intensity distributions indicate that the depth of focus (DOF) for these seven channels is quite deep, measuring approximately 3.5 mm, which is about 100 times the FWHM of the focal point.

Numerical simulation results of reconfigurable OAM beam/comb generation

For multi-channel holography and focusing functionalities, the DMCN utilizes mechanical transformations to dynamically manipulate the intensity of output field. To exploit its capability of complex field manipulation, we further employed the DMCN to generate multi-channel OAM beams and OAM combs. The target OAM beams were set as Laguerre-Gaussian beams, while the target OAM combs were formed by the superposition of multiple orders of OAM beams, which can enhance the parallelism and capacity of communication systems. The waists of the OAM beams were all set to 80 μm , and the complex light fields at the waist planes were taken as the ground truth. The DMCN requires simultaneous optimization of both the amplitude and phase of the output field to achieve complex field manipulation, which introduces an additional phase dimension compared to multi-channel holography and focusing functionalities. Consequently, the number of reconfigurable channels was reduced to 60, approximately half of the aforementioned configurations. Among these 60 channels, 51 were allocated for generating OAM beams with orders ranging from -25 to 25, while the remaining 9 were designated for producing OAM combs formed by combining selected orders of the 51 energy-normalized beams. The optimization targets of these channels are shown in **Supplementary Fig. 23**. The DMCN model was trained with a loss function consisting of the negative correlation coefficient (NCC) of the complex field and the efficiency regularization term (See detailed definition in **Methods**). The layer width of DMCN was set to 300. To improve the purity of the OAM components in the output fields, the FOV width was reduced to 66 and the efficiency hyperparameter η_{Th} was lowered to 3.5%.

Fig. 4 a shows the intensity and phase distributions of the generated 51-channel OAM beams and 9-channel OAM combs. As the order of the OAM beam rises, both the radius of intensity rings and the tangential periodicity of phase profiles expand. OAM combs across different channels display distinct intensity and phase profiles, varying with changes in their constituent orders. The correlation coefficient (CC) matrix of the 51 OAM beams is shown in **Fig. 4 c**. The diagonal elements of this matrix represent the correlation between the output and target beams, with values closely centered around 0.99, indicating the high purity of each OAM beam. The other elements, with values near zero, indicate that the generated OAM beams are uncorrelated, highlighting strong channel orthogonality and negligible crosstalk. **Fig. 4 c** also illustrates the histogram of the 60-channel transmission efficiency, where most channel efficiencies are concentrated around 3.1%. The OAM spectra of the produced 9-channel OAM combs are displayed in **Fig. 4 d**. The definition formula of the spectral coefficients is detailed in the **Methods**. The target OAM comb of the channel 51 includes all orders of OAM beams from -25 to 25. Its output spectrum indicates weaker intensities of the -25th, -6th, 18th, and 24th order component, with coefficients below 0.8. The coefficient for the -22nd order is 1, indicating the strongest intensity, and the coefficients for the other orders

range from 0.8 to 1. Channels 52-55 produce OAM combs formed by the superposition of orders -25 to -16, -15 to -6, -5 to 4, and 5 to 14, respectively. Due to the reduction in the number of orders contained in these combs, the spectral coefficients are more evenly spanned from 0.9 to 1, demonstrating higher intensity consistency across the orders. Channels 56-59 correspond to OAM combs formed by selecting one beam every 2, 3, 4, and 5 orders from the -25 to 25 range. Their OAM spectra show a trend where the low order components at the center have strong intensity, while the intensity of the high order gradually decreases towards the sides.

Experimental results of three functions

Fig. 5 a is the schematic diagram of the experimental optical path. The 532 nm laser underwent multiple reflections within the reflection cavity formed by the SLM and the mirror, being sequentially modulated by the three phase maps of the DMCN. The output light was ultimately captured by a camera at the imaging plane. During the experiment, translation operations were simulated by adjusting the spacing through moving the camera and mirror. Permutation and rotation operations were simulated by respectively exchanging and rotating the phase maps loaded on the SLM. **Fig. 5 b** shows the experimental results of 144-channel holograms, which indicate that the DMCN model can effectively switch between letter images. Compared with numerical simulations, the noise in these letter images is more pronounced, and the differences in image quality among the channels are increased. The PCCs and PSNRs of these images are presented in **Fig. 5 c**. The average PCC drops to 0.8, and the average PSNR decreases to 14.6 dB. The difference between the maximum and minimum PCC increases to 0.124. **Figs. 5 d–e** illustrate the experimental results of 108-channel focus. The single-point focusing shows the best performance, with PCCs around 0.75. The performance of two-point focusing declines due to the enhanced background noise. For three-point and four-point focusing, the background noise is further increased, and uneven focal intensities in some channels (e.g., channels 88, 90, and 102) lead to further degradation in the focusing quality. The average FWHM measures 36.1 μm , similar to the numerical simulation results. **Fig. 5 f** shows the experimental intensity profiles of 60-channel OAM beams/combs. As the topological charge varies, both the ring radius of the OAM beams and the shape of the OAM combs change in accordance with the simulation results. However, the experimentally generated OAM beams exhibit tilted elliptical rings, differing from the ideal donut shape. In addition, high-order OAM beams show noticeable breakage in the ring and significant noise within the ring. We believe this is due to the inherent phase errors of the SLM (for detailed analysis, see **Supplementary Note 5**). Interestingly, the elliptical rings of the positive-order and negative-order OAM beams tilt in symmetric directions, reflecting their opposing phase gradients.

The analysis of five sources of experimental errors and corresponding mitigation strategies are discussed in **Supplementary Note 5**. Although the experimental output fields exhibited a slight reduction in quality compared to the numerical simulations due to these errors, the results clearly demonstrate that our DMCN model is capable of achieving high-capacity reconstruction of light fields within the FOV through mechanical operation adjustments.

The model scalability of DMCN

We selected 288 channels as shown in **Fig. 6 a** and used reconfigurable holography as an example to discuss the relationship between layer width, FOV width, channel number, and PSNR. The average system efficiencies of all simulated models in this section are maintained around 4.5%. To keep the connectivity between adjacent layers, the unit distance interval scales proportionally as the layer width changes. The first line chart shows a linear relationship with a slope of approximately 0.3 between layer width and FOV width, when the number of channels and PSNR are fixed. This indicates that increasing the layer width allows for an enlargement of the output FOV without compromising the model capacity and imaging quality. The relationship between the channel count and PSNR is shown in the second chart. The layer width and FOV width were fixed at 300 and 85, respectively. The image PSNR decreases as the number of optimized channels increases. At 288 channels, the average PSNR is 19.1 dB, which is a 3.7 dB drop compared to 22.8 dB at 144 channels. This trend tells that, with the constant number of trainable model parameters, the channel capacity can be further increased at the expense of imaging quality. In the third and fourth charts, the FOV width is set as 85. We only adjusted the layer width to alter the ratio of layer width to FOV width and analyzed its impact on channel capacity and quality. An expansion in layer width leads to nearly linear growth in the number of channels while preserving a mean PSNR of 22.8 dB. Each 50-unit increase of layer width yields approximately 21 additional channels. Enlarging the layer width also leads to the improvement in image PSNR, with the number of

channels kept constant. If the layer width is below 300, the improvement in image quality is pronounced. However, once it exceeds 300, the rate of improvement slows as the image quality has already reached a high level. Therefore, the information capacity and channel quality of DMCN can be effectively improved by increasing the ratio of layer width to FOV width.

The Channel selection strategy of DMCN

The three types of mechanical transformations enable the DMCN to possess thousands of optimizable channels. However, the limited trainable parameters make it hard to simultaneously optimize such a large number of high-quality channels. Therefore, it is essential to establish a criterion to guide the channel selection process, ensuring that channels with better performance and lower crosstalk are prioritized. This strategy helps maximize the channel capacity while minimizing the impact of channel crosstalk. Taking holography as an example, we analyzed the priority of channel combinations, with the results presented in **Fig. 6 b**. The layer width and FOV width of these models are 300 and 85. The total length of 30 cm is divided into 20 intervals, each measuring 1.5 cm. For translation operations, the distance configuration (10, 5, 5) achieves the highest PSNR of 83 dB among single-channel holography. The PSNR of the dual-channel combination, [(10, 4, 6), (10, 6, 4)], was 8.1 dB higher compared to [(10, 2, 8), (10, 8, 2)]. In four-channel holography, the combination [(6, 6, 8), (7, 7, 6), (8, 8, 4), (9, 6, 5)] achieves approximately twice the PSNR of [(3, 3, 4), (4, 4, 12), (5, 5, 10), (6, 6, 8)]. These results indicate that channels with larger layer spacings are more effective for optimization. Translation operations should prioritize these channels for multiplexing. For rotation operations, whether dual-channel or four-channel combinations were used, the PSNR of the second layer rotation consistently exceeded that of the third layer. Consequently, the second layer should take precedence in rotation to provide multiplexed channels. For permutation operations, dual-channel combinations formed by position exchanges across all three layers achieved significantly higher PSNR compared to those involving two or a single layer. Hence, full permutations of the three layers should take priority for channel generation.

Discussion

In this article, a mechanically-enabled DMCN model is proposed to produce high-quality 144-channel holograms, 108-channel single-focus/multi-focus, and 60-channel OAM beam/comb. The successful implementation of these functions demonstrates that DMCN can manipulate both real-valued field intensities and complex-valued fields, offering exceptionally high information capacity and flexibility. Additionally, channel capacity and quality can be further enhanced by increasing the layer width and the FOV width ratio. Our strategy is highly versatile, as it allows the implementation of various reconfigurable functionalities by simply modifying the loss function. This offers a novel approach to enhancing the capacity of optical information systems. Since the DMCN model only requires simple phase-only modulation units, it can also be implemented using other common devices, such as phase plates. It can also be extended to other spectral bands, including the terahertz and microwave regions. The reconfigurable channels of DMCN are solely formed by mechanical structural variations, making it easy to integrate with other multiplexing strategies such as polarization or wavelength multiplexing to further enhance capacity. Furthermore, the thousands of potential channels available for optimization provide flexible combinations for implementing DMCN. **Supplementary Note 2** discusses the results of diverse combinations in detail.

Our work also has some limitations that require discussion and improvement. The overall size of the implemented DMCN systems and the equivalent numerical aperture of the DMCN focusing system are both constrained by the large pixel size ($\sim 23.5\lambda$) of the SLM. These issues could be addressed by using metasurfaces composed of subwavelength units. Two DMCN models implemented by metasurfaces are discussed in the **Supplementary Note 1**, where the metaatom size is 400 nm and the overall system dimensions are $120\mu\text{m}\times 120\mu\text{m}\times 360\mu\text{m}$. As for OAM applications, the stray fields outside the FOV region need to be filtered out by adding additional spatial filtering apertures at the output plane to ensure that the OAM beam can be transmitted over long distances. High-order OAM beams also require the DMCN to have large layer width and FOV width due to the increase in their ring radius. Two examples of high-order OAM beams and OAM combs generation are provided in the **Supplementary Figs. 16-18**.

The three-layer DMCN models demonstrated in this paper possess 4179 potential channels, and expanding the model to five layers will boost the number of potential channels to approximately 36 million. However, only a few hundred of these channels will be ultimately optimized, meaning that effective information is allocated to fewer than 3% of the potential channels. As a result, retrieving

information from the output plane becomes impossible if the correctly configured channels are unknown. Thus, the DMCN has strong capabilities of encryption and offers promise for realizing novel holographic encryption systems^{38,39}. The reconfigurable focusing system realized by DMCN can accurately switch focal positions and numbers through simple mechanical transformations. Such highly flexible and customizable focusing functionalities will provide a new platform for applications like lithography, microscopy, and optical sensing^{35,40}. By defining appropriate loss functions, the DMCN can dynamically generate OAM beams of any order or OAM combs with arbitrary components and relative intensities. Furthermore, the DMCN can manipulate other complex fields, such as perfect vortex beams, Bessel beams, and Airy beams. This versatility opens up possibilities for generating specialized beams, performing optical beam operations, and enhancing the capacity of optical communication systems⁴¹⁻⁴³. In summary, our DMCN model holds promising prospects for applications in optical computing, optical communication, optical image processing, and optical sensing.

Methods

Forward propagation model of DMCN

The DMCN comprises three phase modulation layers and an output layer. The modulation layers transform the incident wavefield according to the following formula:

$$\begin{aligned} u_l^t(x, y) &= u_l^i(x, y)t_l(x, y) \\ t_l(x, y) &= \exp(j2\pi \text{Sigmoid}(\phi_l(x, y))) \end{aligned} \quad (1)$$

where $u_l^i(x, y)$ and $u_l^t(x, y)$ respectively represent incident and transmitted wave of the l -th layer ($1 \leq l < 3$). $t_l(x, y)$ represents the transmission coefficient of l -th layer and serves as learnable parameters.

Propagation procedure between two adjacent layers can be expressed using the Rayleigh Sommerfeld convolution (RSC)⁴⁵ formula as follows:

$$\begin{aligned} u_{l+1}^i(x, y) &= u_l^t(x, y) * w(x, y, d_l) \\ w(x, y, d_l) &= \frac{d_l}{r^2} \left(\frac{1}{2\pi r} + \frac{j}{\lambda} \right) \exp \left(j \frac{2\pi r}{\lambda} \right) \\ r &= \sqrt{x^2 + y^2 + d_l^2} \end{aligned} \quad (2)$$

Here, d_l ($1 \leq l < 3$) represents the distance between two layers, and $w(x, y, d_l)$ is the convolution operator that captures the diffraction connections.

Although the RSC method can accurately depict the light diffraction process in DMCN, the computational overhead caused by large-kernel convolutions makes it impractical for model training. Therefore, we only utilized this equation for numerical validation. Instead, a lower-computing and faster algorithm known as angular spectrum method (ASM)⁴⁵ was employed for model training and inference, which can be expressed as follows:

$$\begin{aligned} u_{l+1}^i(x, y) &= \text{IFFT}(\text{FFT}(u_l^t(x, y))H(f_x, f_y, d_l)) \\ H(f_x, f_y, d_l) &= \exp \left(\frac{j2\pi d_l}{\lambda} \sqrt{1 - (\lambda f_x)^2 - (\lambda f_y)^2} \right) \end{aligned} \quad (3)$$

where $H(f_x, f_y, d_l)$ is the spectrum transfer function, f_x and f_y are spatial frequencies along x and y axis, respectively.

The mechanically reconfigurable non-orthogonal channels of DMCN

The multiplexing channels of DMCN are realized through the combination of three types of mechanical operations: rotation, permutation, and translation. To theoretically demonstrate the reconfigurable principle, we derived the output wavefield of DMCN in compact form under the plane wave illumination by discretizing equations (1) and (2).

$$\text{Vec}(\mathbf{O}_c) = \mathbf{W}(d_3) \text{Diag}(\text{Rot}(\mathbf{T}_3, \Omega_2)) \mathbf{W}(d_2) \text{Diag}(\text{Rot}(\mathbf{T}_2, \Omega_1)) \mathbf{W}(d_1) \text{Diag}(\mathbf{T}_1) \text{Vec}(\mathbf{J}) \quad (4)$$

Here, \mathbf{J} is the all-one matrix that represents the input plane wave, \mathbf{T}_l is the transmission coefficient matrix and $\mathbf{W}(d_l)$ is the diffraction matrix composed of convolutional kernels. $\text{Vec}(\cdot)$ operator flattens the matrix into column vector. $\text{Diag}(\cdot)$ operator transforms all elements of the matrix into a diagonal vector, thereby forming a diagonal matrix. $\text{Rot}(\cdot, \cdot)$ operator rotates the matrix counterclockwise

by a certain angle.

From equation (4), the transfer matrix of DMCN can be further derived as follows:

$$\mathbf{A}_c = \mathbf{W}(d_3)\text{Diag}(\text{Rot}(\mathbf{T}_3, \Omega_2))\mathbf{W}(d_2)\text{Diag}(\text{Rot}(\mathbf{T}_2, \Omega_1))\mathbf{W}(d_1)\text{Diag}(\mathbf{T}_1) \quad (5)$$

This transfer matrix is solely determined by the system parameters and is independent of the input. The parameters Ω_1 and Ω_2 are adjusted through rotation, while d_1 , d_2 and d_3 are controlled by translation. The permutation operation alters the order of the three transmission layers, thereby affecting the values of \mathbf{T}_1 , \mathbf{T}_2 and \mathbf{T}_3 . Each operation can modify the transfer matrix, generating a new non-orthogonal channel. These channels are capable of performing different tasks with the same input.

Loss function and evaluation criteria

We employed the following loss function to train the DMCN.

$$\mathcal{L}_{DMCN} = \mathcal{L}_{Err} + \gamma_{Eff} \mathcal{L}_{Eff} \quad (6)$$

Here, \mathcal{L}_{Err} quantifies the error between the output and target wavefields. For hologram and focus applications, this term is defined as mean square error (MSE).

$$\begin{aligned} \mathcal{L}_{Err} = \mathcal{L}_{MSE} &= \frac{1}{N} \sum_{c=1}^N E[|\sigma_1 G_c(x, y) - \sigma_2 O_c(x, y)|^2] \\ \sigma_1 &= \frac{1}{\sum_{(x,y) \in FOV_0} G_c(x, y)} \\ \sigma_2 &= \sigma_1 \frac{\sum_{(x,y) \in FOV_0} G_c(x, y) |O_c(x, y)|^2}{\sum_{(x,y) \in FOV_0} |O_c(x, y)|^4} \end{aligned} \quad (7)$$

In these equations, $E[\cdot]$ is the average operator, while $G_c(x, y)$ and $O_c(x, y)$ stand the training target and the output wavefield of the c -th channel, respectively. N is the number of channels. σ_1 and σ_2 are normalization factors.

For OAM application, \mathcal{L}_{Err} is defined as negative correlation coefficient of complex fields.

$$\mathcal{L}_{Err} = \mathcal{L}_{NCC} = \frac{1}{N} \sum_{c=1}^N \frac{-|\sum_{(x,y) \in FOV_0} G_c(x, y) O_c^*(x, y)|}{\sqrt{\sum_{(x,y) \in FOV_0} |G_c(x, y)|^2 \sum_{(x,y) \in FOV_0} |O_c(x, y)|^2}} \quad (8)$$

The term \mathcal{L}_{Eff} is a regularization factor designed to ensure system efficiency, defined as:

$$\begin{aligned} \mathcal{L}_{Eff} &= \frac{1}{N} \sum_{c=1}^N \mathcal{L}_{SubEff}^c \\ \mathcal{L}_{SubEff}^c &= \begin{cases} -\ln\left(\frac{\eta_c}{\eta_{Th}}\right), & \eta_c < \eta_{Th} \\ 0, & \eta_c \geq \eta_{Th} \end{cases} \\ \eta_c &= \frac{\sum_{(x,y) \in ROI} |O_c(x, y)|^2}{\sum_{(x,y)} |J(x, y)|^2} \end{aligned} \quad (9)$$

where η_c represents the efficiency of the c -th channel, η_{Th} is a hyperparameter that specifies the target efficiency, and $J(x, y)$ denotes the input plane wave. The region of interest (ROI) corresponds to FOV_0 for hologram and OAM applications, and to the target focus region for focus applications. γ_{Eff} is the weight coefficient for the efficiency regulation term, which was set as 0.01 for all models.

For hologram and focus evaluation, we further took the PCC and PSNR as metrics, which are defined as follows:

$$PCC(G(x, y), O(x, y)) = \frac{\sum_{(x,y)} (G(x, y) - E[G(x, y)])(O(x, y) - E[O(x, y)])}{\sqrt{\sum_{(x,y)} |G(x, y) - E[G(x, y)]|^2 \sum_{(x,y)} |O(x, y) - E[O(x, y)]|^2}} \quad (10)$$

$$PSNR(G(x, y), O(x, y)) = 10 \log_{10} \frac{1}{E[|\tilde{G}(x, y) - \tilde{O}(x, y)|^2]} \quad (11)$$

where $\tilde{\cdot}$ is the max-normalization operator.

Lastly, the normalized OAM coefficients defined as follows were employed to analyze the OAM components contained in generated combs:

$$\begin{aligned} C_l &= \int_0^\infty \left[\int_0^{2\pi} O(r, \varphi) \exp(-il\varphi) d\varphi \right]^2 r dr \\ \tilde{C}_l &= \frac{C_l}{\max_{-\infty < l < \infty} C_l} \end{aligned} \quad (12)$$

where $O(r, \varphi)$ is the output field in spherical coordinate.

Numerical and Experimental implementations

Our numerical DMCN models were implemented using Python and PyTorch on a workstation equipped with a Xeon® Gold 6430 CPU and a GeForce RTX 4090 GPU. The original pixel size of all the numerical models was set to $12.5 \mu\text{m}$. To reduce numerical computation errors, we enhanced the spatial sampling rate by applying two-times upsampling for each pixel and improved the spectral sampling rate of the FFT by zero-padding to four times the original length. During each training iteration, the full batch containing all channel data pairs was fed into the model. And the Adam optimizer with a learning rate of 0.1 was used for backpropagation (BP) to update the transmission coefficients of the DMCN. The training procedure last around 15 minutes, involving 4000 epochs to ensure sufficient optimization.

For the experimental setup, a Verdi V6 laser was employed to generate incident light with a wavelength of 532 nm. A mirror with a side length of 9 mm and a LCOS-SLM X13138-01 type SLM were used to construct a reflection cavity. The SLM has a pixel size of $12.5 \mu\text{m}$ and a panel resolution of 1024×1272 . To accurately direct the laser beam to the designated position on the SLM and facilitate subsequent adjustments to minimize errors, the laser beam was set at an incidence angle of around 3.5° . The initial incidence point was positioned 2.75 mm from the edge of the SLM panel. Each diffraction layer used in the experiment was square-shaped with a side length of 3.75 mm , corresponding to a 300×300 pixel area on the SLM. To satisfy the experimental parameter requirements, the distance between the mirrors and the SLM was set to $d = 3.25 \text{ mm} \sim 3.75 \text{ mm}$. This range ensures that the diffracted light originating from a corner pixel of the first layer on the SLM can precisely reach the opposite corner pixel of the third layer without altering the relative positions of the laser beam and the SLM. With above setup, the input beam underwent two reflections on the mirrors, enabling the beam to propagate through the three-layer DMCN. After the third diffraction by the SLM, the resulting imaging pattern was captured by a Complementary Metal-Oxide-Semiconductor (CMOS) camera. The CMOS camera features a pixel size of $3.45 \mu\text{m}$ and a resolution of 1440×1080 . The captured beam occupied an area of 834×834 pixels on the CMOS sensor. To minimize errors caused by lateral and longitudinal misalignment, the double-nested lens phase patterns proposed by Ghahremani et al. were loaded onto the SLM, and alignment could be performed based on the far-field diffraction patterns⁴⁵.

Disclosures

The authors declare no competing interests.

Code and Data Availability

The deep learning models reported in this work used standard libraries and scripts that are publicly available in PyTorch. All the data and methods needed to evaluate the conclusions of this work are presented in the main text and Supplementary Materials. Additional data can be requested from the corresponding author.

Acknowledgements

The authors acknowledge the financial support by the National Natural Science Foundation of China (Grants No.61991423).

References

1. Arbabi, A., Horie, Y., Bagheri, M. & Faraon, A. Dielectric metasurfaces for complete control of phase and polarization with subwavelength spatial resolution and high transmission. *Nat. Nanotechnol* 10, 937-943 (2015).
2. Wang, B. et al. Visible-Frequency Dielectric Metasurfaces for Multiwavelength Achromatic and Highly Dispersive Holograms. *Nano Lett.* 16, 5235-5240 (2016).
3. He, J., Ye, J., Wang, X., Kan, Q. & Zhang, Y. A broadband terahertz ultrathin multi-focus lens. *Sci. Rep.* 6, 28800 (2016).
4. Liu, Z. et al. Broadband, Low-Crosstalk, and Massive-Channels OAM Modes De/Multiplexing Based on Optical Diffraction Neural Network. *Laser Photonics Rev.* 17 (2023).

5. Chong, M.-Z. et al. Generation of polarization-multiplexed terahertz orbital angular momentum combs via all-silicon metasurfaces. *Light: Adv. Manuf.* 5 (2024).
6. Yuan, Y. et al. Independent phase modulation for quadruplex polarization channels enabled by chirality-assisted geometric-phase metasurfaces. *Nat. Commun.* 11, 4186 (2020).
7. Lin, X. et al. All-optical machine learning using diffractive deep neural networks. *Science* 361, 1004-1008 (2018).
8. Ding, X. et al. Metasurface-Based Optical Logic Operators Driven by Diffractive Neural Networks. *Adv. Mater.* 36, e2308993 (2024).
9. Zhao, Z. et al. Deep learning-enabled compact optical trigonometric operator with metasurface. *Photonix* 3 (2022).
10. Fan, Z. et al. Holographic multiplexing metasurface with twisted diffractive neural network. *Nat. Commun.* 15, 9416 (2024).
11. Huang, Y. W. et al. Aluminum plasmonic multicolor meta-hologram. *Nano Lett.* 15, 3122-3127 (2015).
12. Luo, X. et al. Metasurface-enabled on-chip multiplexed diffractive neural networks in the visible. *Light Sci. Appl.* 11, 158 (2022).
13. Xu, H.-X. et al. Completely Spin-Decoupled Dual-Phase Hybrid Metasurfaces for Arbitrary Wavefront Control. *ACS Photonics* 6, 211-220 (2018).
14. Balthasar Mueller, J. P., Rubin, N. A., Devlin, R. C., Groever, B. & Capasso, F. Metasurface Polarization Optics: Independent Phase Control of Arbitrary Orthogonal States of Polarization. *Phys. Rev. Lett.* 118, 113901 (2017).
15. Ren, H. et al. Metasurface orbital angular momentum holography. *Nat. Commun.* 10, 2986 (2019).
16. Chen, K. et al. Directional Janus Metasurface. *Adv. Mater.* 32, e1906352 (2020).
17. Wan, S., Tang, J., Wan, C., Li, Z. & Li, Z. Angular-Encrypted Quad-Fold Display of Nanoprinting and Meta-Holography for Optical Information Storage. *Adv. Opt. Mater.* 10 (2022).
18. Xiong, B. et al. Breaking the limitation of polarization multiplexing in optical metasurfaces with engineered noise. *Science* 379, 294-299 (2023).
19. Wang, Y., Pang, C. & Qi, J. 3D Reconfigurable Vectorial Holography via a Dual-Layer Hybrid Metasurface Device. *Laser & Photonics Rev.* 18 (2023).
20. Wang, Y., Yu, A., Cheng, Y. & Qi, J. Matrix Diffractive Deep Neural Networks Merging Polarization into Meta-Devices. *Laser & Photonics Rev.* 18 (2023).
21. Wang, J. et al. Unlocking ultra-high holographic information capacity through nonorthogonal polarization multiplexing. *Nat. Commun.* 15, 6284 (2024).
22. Liu, C. et al. A programmable diffractive deep neural network based on a digital-coding metasurface array. *Nat. Electron* 5, 113-122 (2022).
23. Li, L. et al. Electromagnetic reprogrammable coding-metasurface holograms. *Nat. Commun.* 8, 197 (2017).
24. Zhang, X. G. et al. An optically driven digital metasurface for programming electromagnetic functions. *Nat. Electron* 3, 165-171 (2020).
25. Chen, B. et al. Directional terahertz holography with thermally active Janus metasurface. *Light Sci. Appl.* 12, 136 (2023).
26. Wang, Z. et al. Origami-Based Reconfigurable Metamaterials for Tunable Chirality. *Adv. Mater.* 29 (2017).
27. Zheng, Y. et al. Chirality-Switching and Reconfigurable Spin-Selective Wavefront by Origami Deformation Metasurface. *Laser & Photonics Rev.* 18 (2023).
28. Han, D. et al. Kirigami-Inspired Planar Deformable Metamaterials for Multiple Dynamic Electromagnetic Manipulations. *Laser & Photonics Rev.* 17 (2023).
29. Zheng, Y. et al. Kirigami Reconfigurable Gradient Metasurface. *Adv. Funct. Mater.* 32 (2021).
30. Wang, H. et al. Origami-Kirigami Arts: Achieving Circular Dichroism by Flexible Meta-Film for Electromagnetic Information Encryption. *Laser & Photonics Rev.* 17 (2022).
31. He, G. et al. Twisted Metasurfaces for On-Demand Focusing Localization. *Adv. Opt. Mater.* (2024).
32. Zhang, X. et al. Switchable Diffraction Pattern Based on Cascaded Metasurfaces. *Laser & Photonics Rev.* 18 (2024).
33. He, C. et al. Pluggable multitask diffractive neural networks based on cascaded metasurfaces. *Opto-Electron. Adv.* 7, 230005-230005 (2024).

34. Wei, Q. et al. Rotational Multiplexing Method Based on Cascaded Metasurface Holography. *Adv. Opt. Mater.* 10 (2022).
35. Wang, X. et al. 3D Nanolithography via Holographic Multi-Focus Metalens. *Laser & Photonics Rev.* 18 (2024).
36. Wu, Y. et al. Tbps wide-field parallel optical wireless communications based on a metasurface beam splitter. *Nat. Commun.* 15, 7744 (2024).
37. Li, W., Yu, Q., Qiu, J. H. & Qi, J. Intelligent wireless power transfer via a 2-bit compact reconfigurable transmissive-metasurface-based router. *Nat. Commun.* 15, 2807 (2024).
38. Georgi, P. et al. Optical secret sharing with cascaded metasurface holography. *Sci. Adv* 7, eabf9718 (2021).
39. Guo, X. et al. Stokes meta-hologram toward optical cryptography. *Nat. Commun.* 13, 6687 (2022).
40. Suresh, S. A. et al. All-Dielectric Meta-Microlens-Array Confocal Fluorescence Microscopy. *Laser & Photonics Rev.* (2024).
41. Deng, M. et al. Broadband angular spectrum differentiation using dielectric metasurfaces. *Nat. Commun.* 15, 2237 (2024).
42. Wen, J. et al. All-Dielectric Synthetic-Phase Metasurfaces Generating Practical Airy Beams. *ACS Nano* 15, 1030-1038 (2021).
43. Wang, J. et al. Terabit free-space data transmission employing orbital angular momentum multiplexing. *Nat. Photonics* 6, 488-496 (2012).
44. Zhang, W., Zhang, H., Sheppard, C. J. R. & Jin, G. Analysis of numerical diffraction calculation methods: from the perspective of phase space optics and the sampling theorem. *J Opt Soc Am A Opt Image Sci Vis* 37, 1748-1766 (2020).
45. Ghahremani, M., McClung, A., Mirzapourbeinekalaye, B. & Arbabi, A. 3D alignment of distant patterns with deep-subwavelength precision using metasurfaces. *Nat. Commun.* 15, 8864 (2024).

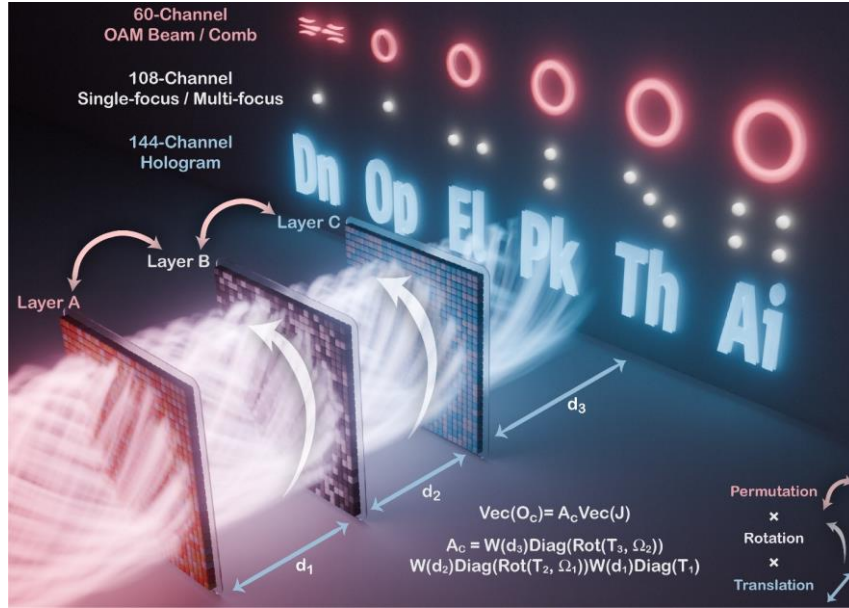


Fig. 1 | Schematic of DMCN. The DMCN consists of three phase-only modulation layers. Using the D^2NN model to describe the wave propagation process, we derived the channel system matrix \mathbf{A}_c (See **Methods** for details). Each mechanical operation introduces a variation to the formula of \mathbf{A}_c , thereby generating new channels. Specifically, permutation alters the correspondence between $\mathbf{T}_1, \mathbf{T}_2, \mathbf{T}_3$ and layers A, B, and C. Rotation modifies the values of Ω_1 and Ω_2 . Translation changes the values of d_1, d_2, d_3 . Consequently, simple combinations of mechanical operations create thousands of potential channels. By assigning different optimization objectives, we respectively achieved 144-channel holograms, 108-channel single-foci/multi-foci, 60-channel OAM beam/comb generation.

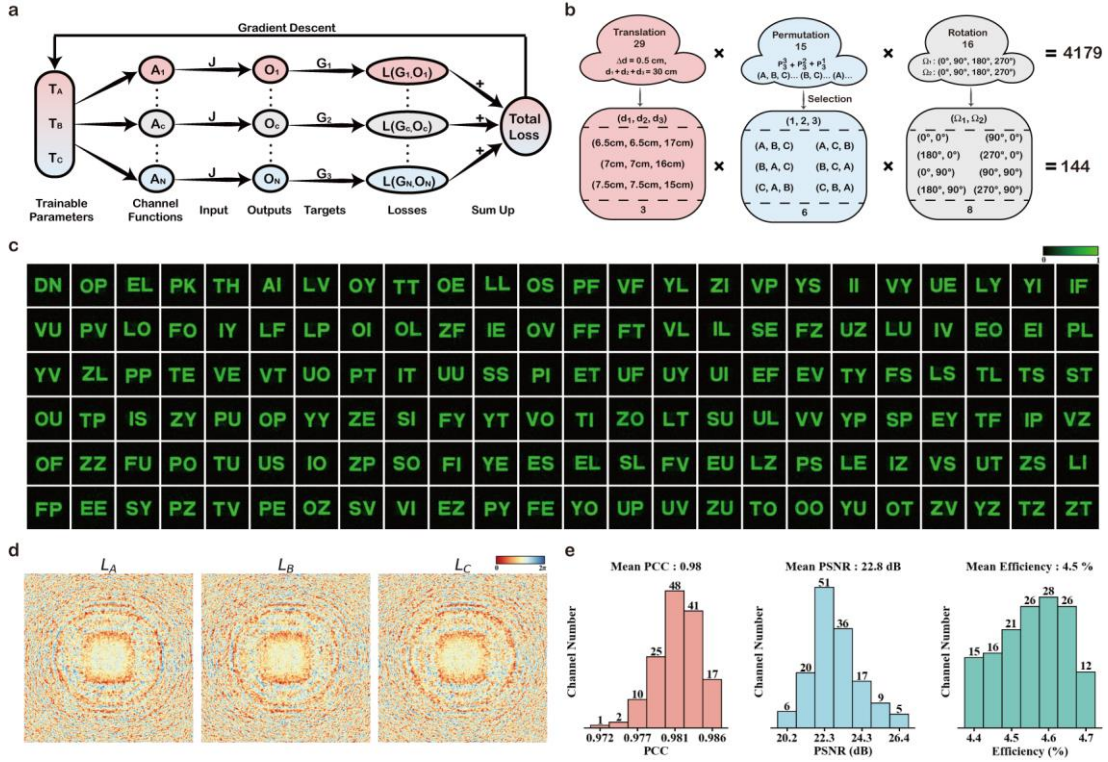


Fig. 2 | Multi-channel optimization algorithms and simulation results of holography. **a** The joint optimization procedure of multiple channels. T_A, T_B, T_C are set as trainable parameters, which are shared by all channels generated through mechanical reconfiguration. During each iteration, the loss for each channel is computed individually and aggregated, after which gradient descent is applied to update the parameters. **b** Potential and selected channels. The permutation, rotation, and translation respectively generate 16, 15, and 29 channels, being combined to generate 4179 channels ($P_m^n = \frac{m!}{(m-n)!}$). 144 channels to be optimized are carefully selected from them. **c** Hologram results of 144-channel letter images. **d** Three-layer phase profiles of DMCN. **e** Metric distribution histogram of the 144-channel holograms.

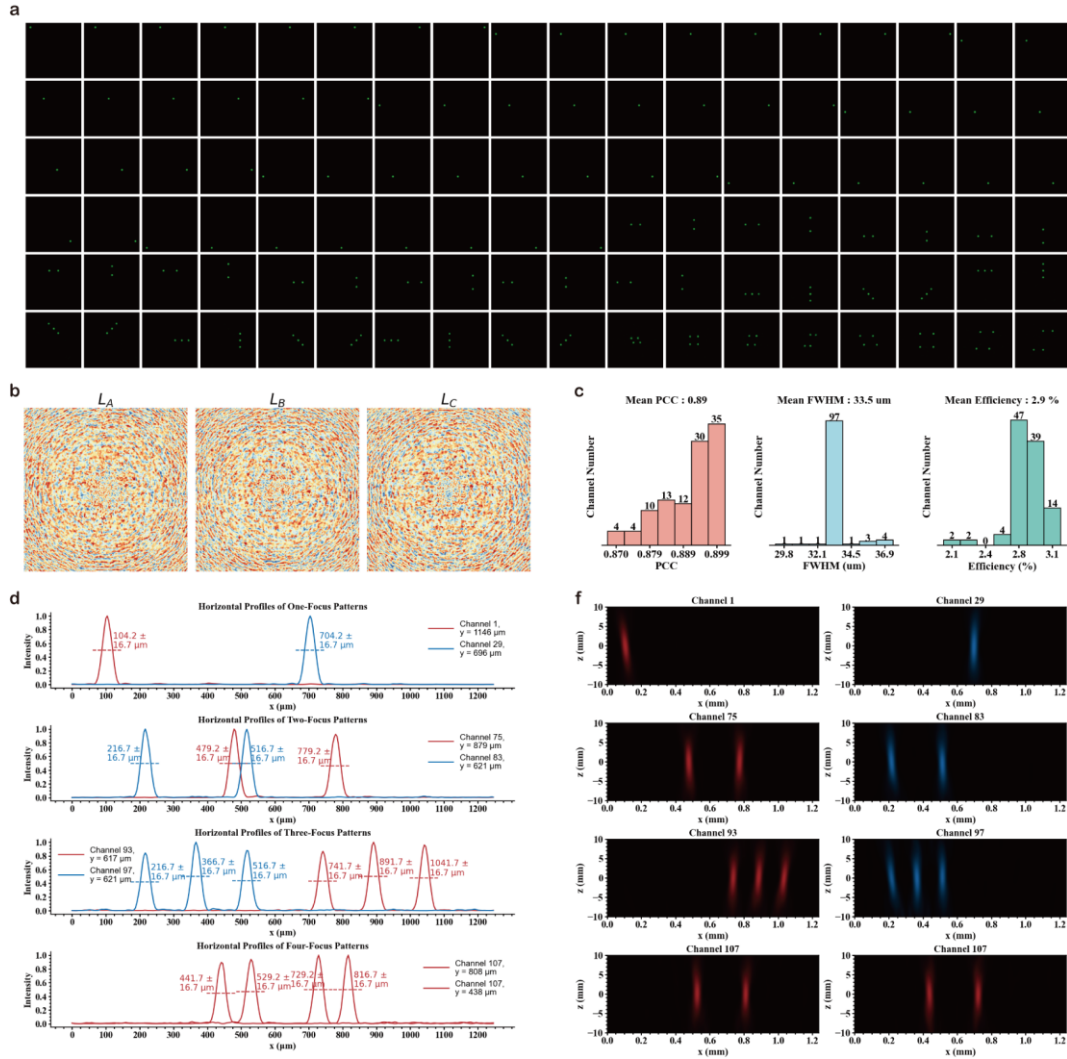


Fig. 3 | Simulation results of 108-channel mechanically reconfigurable single-focus/multi-focus. **a** Focusing results of 108-channel single-focus/multi-focus. **b** Three-layer phase profiles of DMCN. **c** Metric distribution histogram of the single-focus/multi-focus. **d** one-dimensional horizontal profiles of the focal heights at the focal plane for 7 channels. Channel 1 and 29 are single-focus channels, channel 75 and 83 are dual-focus channels, channel 93 and 97 are triple-focus channels, and channel 107 is a quadruple-focus channel. **e** two-dimensional horizontal cross-sections of the focal heights for 7 channels. Focal plane locates at $Z = 0$ mm.

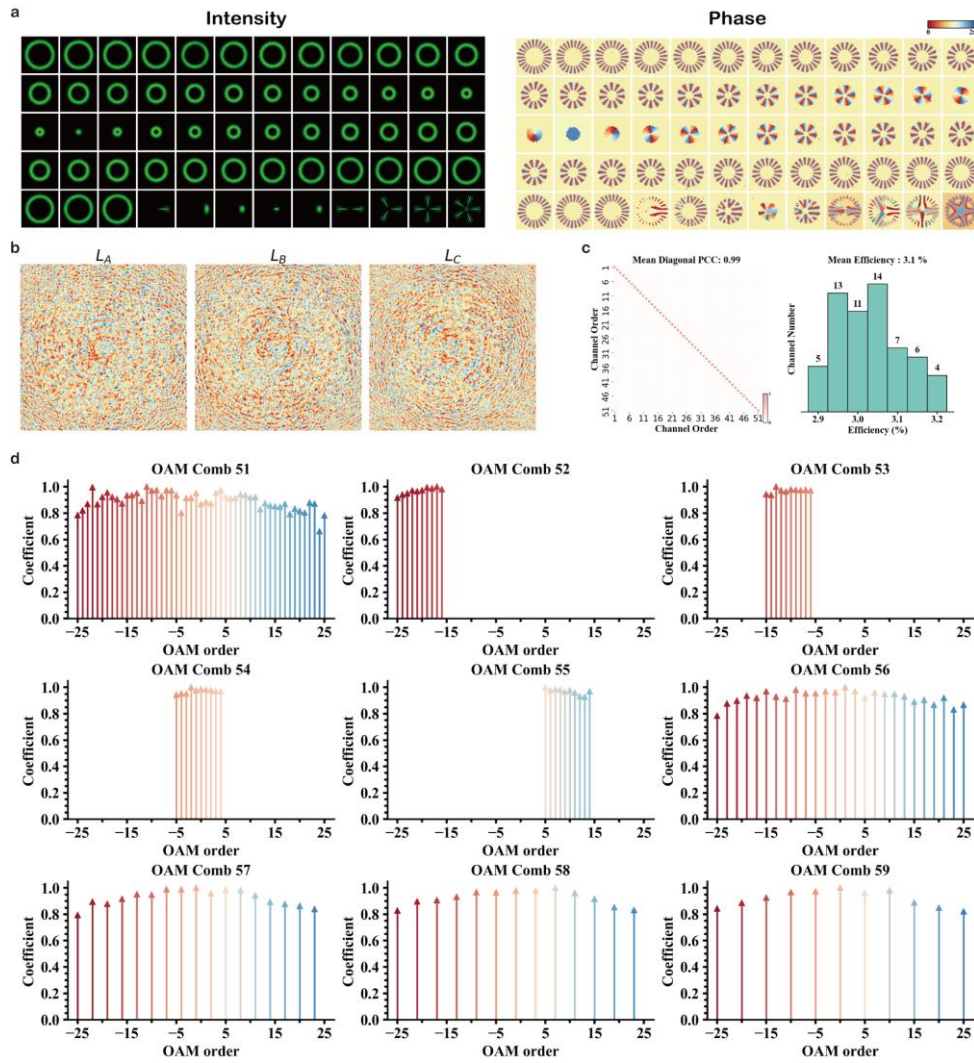


Fig. 4 | Simulation results of 60-channel mechanically reconfigurable OAM beam/comb generation. a. Intensity and phase distributions of produced 60-channel OAM/comb. **b** Three-layer phase profiles of DMCN. **c** CC matrix of generated 51-channel OAM and efficiency histogram of all channels. **d** Normalised OAM coefficient distributions of generated 9-channel OAM combs.

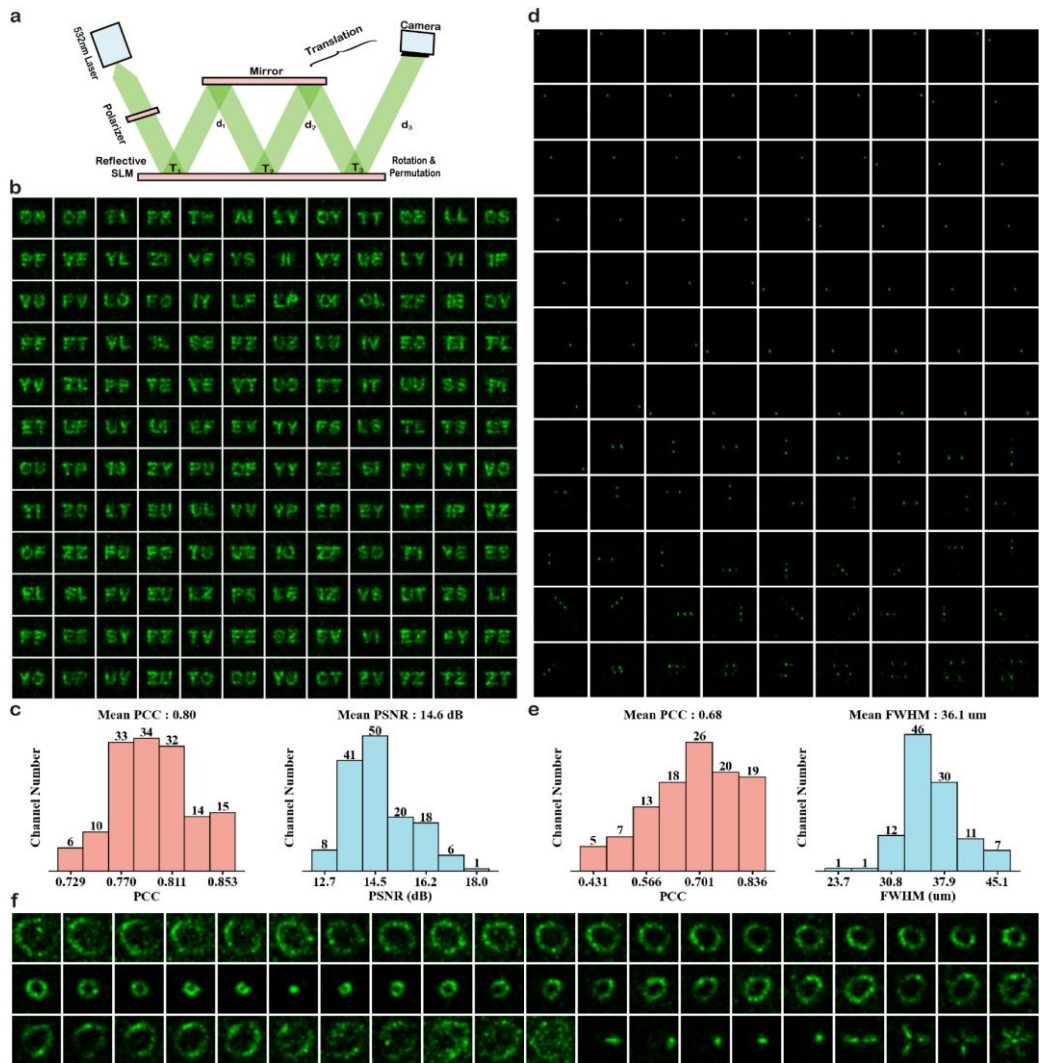


Fig. 5 | Experimental validations of DMCN models. **a** Experimental optical path diagram. 532nm laser reflected three times between the SLM and mirrors before reaching the CCD for imaging. **b-c** Experimental results of 144-channel holograms. **d-e** Experimental results of 108-channel single-focus/multi-focus. **f** Intensity distributions of experimentally generated 60-channel OAM beam/comb.

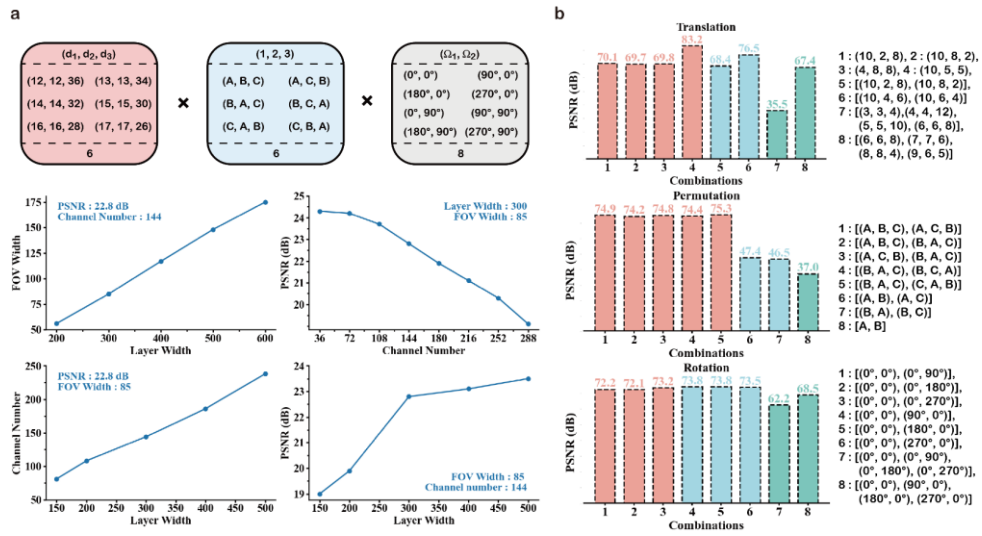


Fig. 6 | Parameter discussion of DMCN based on reconfigurable holography. a Line charts analyzing the relationships among Layer Width, FOV Width, PSNR, and Channel Number, based on the selected 288 channels. The letter images are used as target holograms. We employ the controlled variable method, fixing the values of two variables while discussing the interactions between the other two. **b** Comparative bar chart for different combinations of a single mechanical operation. The Quick Draw images are used as target holograms. These results form the basis for the channel selection strategy.